Reprinted from JOURNAL OF ATMOSPHERIC AND OCEANIC TECHNOLOGY, Vol. 12, No. 3, June 1995
American Meteorological Society

Directional Surface Wave Estimates from Doppler Sonar Data

JEROME A. SMITH AND GREGORY T. BULLARD

Scripps Institution of Oceanography, University of California, San Diego, La Jolla, California

(Manuscript received 28 March 1994, in final form 21 November 1994)

ABSTRACT

A quick analysis for deriving directional-frequency spectra from surface grazing Doppler sonar data is presented. Here, "quick" refers to both the short time span of data required and computational ease. The technique employs time and space Fourier transforms to estimate the frequency-wavenumber power content for each sonar beam. The directional information is converted into the first four circular Fourier components at each frequency (including the mean power estimate), to facilitate rotation to true North coordinates. The motivation is to estimate the lowest few circular Fourier components of the directional wave distribution robustly and efficiently, without reducing the statistical stability afforded by the spatial extent of the array. Several potential difficulties inherent to Doppler sonar data are discussed in some detail; the quick analysis is robust with respect to these concerns. Using data from SWAPP (the Surface WAve Process Program), the quick analysis results are compared to those from a 3-wire array. The directional components are estimated with reasonable statistical stability from 13 minute segments: e.g., the mean wave direction has an RMS error of about 6°. Comparable accuracy from the wire array requires averaging for about four times as long.

1. Introduction

Time series of directional wave characteristics have proven difficult to obtain in the open ocean. A workhorse of most such data sets to date has been the tilt and roll buoy. While much progress can be attributed to the use of these devices, there are clear advantages to having either higher resolution measurements of the waves, or comparable detail with less averaging time. On the high-resolution side, measurements taken from airplanes and satellites (for example) tend to be isolated "snap shots" in time, which make it difficult to piece together the temporal evolution of the wave field. Here, data from a Doppler sonar system are considered. This system can provide continual wave measurements for the duration of an experiment. For example, it was deployed for over 20 days as part of the "Surface Wave Process Program" (SWAPP).

The objective of SWAPP was to measure surface waves and wave related flows in the mixed layer, and to relate these to forcing by buoyancy fluxes, wind stress, preexisting stratification, and other environmental factors. As part of this program, the research platform FLIP (Floating Instrument Platform) was moored at 35°N, 127°W, roughly 500 km off the coast of California, from February 24, 1990, through 18 March 1990 (Figure 1). The R/P FLIP is 108 m long or, when vertical, 90 m deep. When vertical, it is a stable platform from which oceanographic measurements can be made. The focus here is on data taken from FLIP with a high-resolution sonar system (the "HR sonar"), operated at 195kHz acoustic center frequency, and having about 400 m maximum range. We also have data from several other sonars, a three-wire wave staff array, and from variety of motion sensing devices including accelerometers and a three-component magnetic flux-gate. The Canadian vessel CSS *Parizeau*, the US Navy tugboat *Navajo*, and the R/V *DeSteiguer* were also involved in coordinated scientific studies. A wide variety of other oceanographic and meteorological measurements were made; see Weller et al (1991) for a complete description. Over the course of the experiment, several wind events were encountered, of which three had sustained winds over 12 m/s (Figure 2).

In general, motion of the supporting platform affects the measurements. The quick analysis presented here is insensitive to the small motions of FLIP. This method provides modestly detailed directional information within a very short time (of order 3–10 min) from Doppler sonar data. The results of this analysis are compared to spectra derived from a resistance wire array, one of several kinds of supporting data obtained during SWAPP. The comparisons indicate that the quick analysis produces accurate directional spectra for wave periods between 2 and 14 s, from 10 to 15 min of data. This combination of equipment and analysis permits the examination of the temporal evolution of the directional wave spectrum under rapidly changing

Corresponding author address: Jerome A. Smith, Marine Physical Laboratory, Scripps Institution of Oceanography, 9599 Gilman Dr., La Jolla, CA 92093-0213.
E-mail: jasmith@ucsd.edu

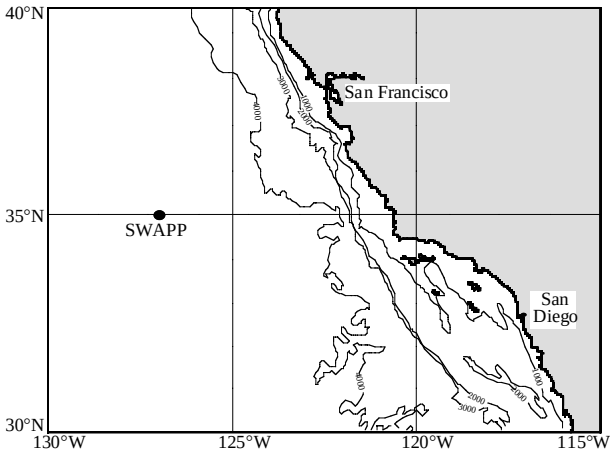

Fig. 1. Location of SWAPP site. SWAPP took place in February and March 1990, at 35°N, 127°W, about 500 km off the coast of California. The ocean bottom at the site is flat, and the depth is roughly 4000 m.

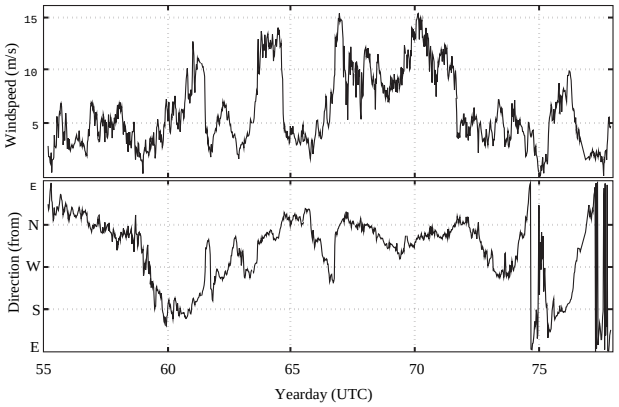

Fig. 2. Wind speed and direction, yeardays 55 to 77 (Feb. 24 to March 18), 1990 (Wind data provided by A. Plueddemann and R. Weller, Woods Hole Oceanographic Institution.).

wind conditions. The data could alternatively be analyzed to produce higher-resolution directional information, with correspondingly longer averaging times required to achieve statistical stability. Discussion of this latter course of action is deferred.

Similar sonar configurations have been deployed in a variety of situations, but with two or even just one beam. For example, two-beam systems have been deployed previously from FLIP (Pinkel and Smith 1987), from an oil platform (Krogstad et al. 1988), from a subsurface buoy (Trevorrow and Farmer 1992), and on the bottom (e.g., Thorpe and Hall 1983). A one-beam system was deployed at the end of a pier (Smith 1993). High advection velocities associated with moving ships make them less attractive platforms for this purpose; significant reworking of the analysis would be required. The analysis described here can be applied to data from two or more sonar beams. The number of circular Fourier components estimated equals the number of beams. Thus, with two beams it can be used to estimate the mean momentum and direction of the wavefield versus frequency.

2. Doppler Sonar Configuration

Four Doppler sonar systems were deployed on the *R/P FLIP* for the duration of SWAPP. Of these, two were designed and operated to monitor surface velocities (Smith 1989) to track both surface wave directional spectra and lower frequency motions such as Langmuir circulation (Smith 1992). One, operated at 195 kHz, had better range resolution (3 m) but less total range (~400 m). This "high-resolution" (HR) system consisted of 4 beams at 45° increments (see Figure 3). The analysis described here uses only the HR sonar data.

The echoes at 195kHz acoustic frequency are dominated by backscatter from bubbles. The resonant bubble size is about 15μm. The vertical extent of the measurement volume is confined by the form of the near-surface bubble layer and bubble clouds (Figure 4). The intensity of the backscatter from bubbles can vary by a factor of 1000 from spot to spot, and as conditions change. However, the bubbles remain strongly surface trapped, both inside and outside the denser bubble clouds. The profile is believed to be roughly equivalent to exponential decay, having a depth scale of about 1–1.5 m (Crawford and Farmer 1987, Thorpe 1986). This bubble layer is continuous in winds over 3–4 m s^{-1} and dominates the backscatter signal. The surface-scanning Doppler sonars have beam patterns that are narrow azimuthally, but broad in the vertical (about

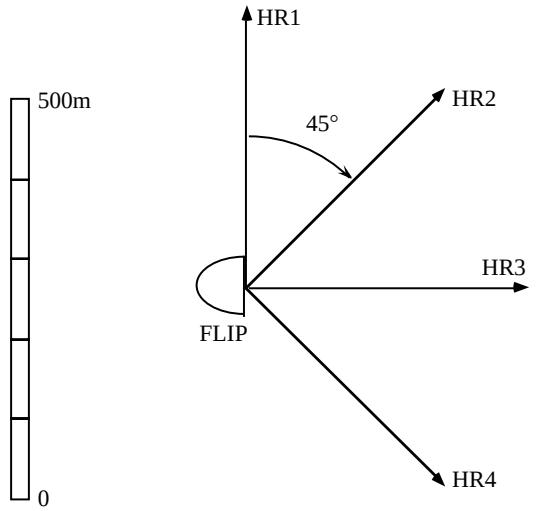

Fig. 3. Plan view of the 4 surface-scanning "high resolution" (HR) Doppler sonar beams, roughly to scale (except for FLIP itself). The system measured intensity and Doppler shift of a 195kHz carrier signal backscattered from bubbles in "range bins" spaced every 3 m out to 400 m from FLIP.

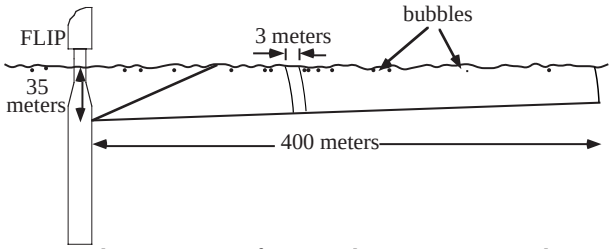

Fig. 4. Schematic view of a sonar beam intersecting the near surface bubble cloud. The bubbles decrease in number with depth, with roughly an exponential profile. The depth scale of the decay is about 1 to 1.5 m. Acoustic backscatter from the bubble cloud completely dominates the return.

2/3° wide by 22° in the vertical, for the HR sonar). The vertical extent of the measurements is presumably set by the geometry of the bubble clouds, and thus extends a meter or two downward from the surface, with an acoustic centroid near 1 m depth. Considering the exponential decay of wave motions with depth, and the order 1 m depth scale of the bubble layer, the short wave cutoff for this sonar configuration lies near 6 m wavelength (2 second periods).

The extent of the measurement volume in range is determined by the duration of transmitted pulse and the amount of range averaging (both corresponding to 3 m for the HR system), while the azimuthal dimension is set by the narrow azimuthal beam width (e.g., at 250 m, 2/3° corresponds to about 3 m). This overall beam geometry minimizes sensitivity to pitch and roll of the platform, while maintaining measurement volumes of about $(3\ m)^3$ just below the ocean surface. The measurement volume follows the vertical excursions of the fluid near the surface, to the extent allowed by geometry (i.e., shadowing). The resulting measurements are semi-Lagrangian, following fluid parcels in the vertical but not in the horizontal directions.

Velocity estimates were formed by the standard complex autocovariance technique, as modified for incoherent, repeat-sequence coded sonars (Pinkel and Smith 1992). The HR sonars transmitted a 4-bit repeat-sequence code every 0.75 s. Covariance estimates were averaged in range for 4 ms (3 m), yielding an estimated rms error of about 12 cm/s in each range bin per transmission (ping). Recording every ping allows the surface wave directional spectrum to be estimated. To examine the underlying lower frequency motions, 1-min averages of the velocity data were also formed. For most of the experiment, data collection alternated hourly between "wave-mode" runs, in which every ping is recorded (52-min duration), and Langmuir circulation or "LC-mode" runs, recording just 1-min averages (68 min). During the initial 8 h of a wind event on year-day 63 (March 4), and for the first 16 h of a wind event on year-day 67 (March 8), wave-mode data were collected continuously, to facilitate study of wave growth and wave-current interactions.

3. A Quick Directional Algorithm

The analysis technique described here is intended to provide estimates of wave directional frequency spectra from relatively short time segments, with high computational efficiency. It is useful to describe the strategy first, then the analysis, and then to consider the potential weaknesses and how these affect the results.

a. Strategy

The HR sonar provides velocity estimates at almost 600 locations each 0.75 seconds. A first step in the analysis of data from such a large array is almost always the choice of how to reduce the number of data points to a manageable level. For example, Krogstad et al. (1988) use a matrix pivoting technique to select a subset of suitably distinct locations. The resulting collection of spatial lags requires an hour's worth of averaging to achieve statistical stability. Here a different strategy is used, based on the following: From a single transmission, the spatial lags aligned with a sonar beam have multiple realizations (displaced slightly along the beam), which can be averaged together to provide additional degrees of freedom. In contrast, any spatial lag involving two different beams has no other exact match, and so no spatial averaging is possible. Additional statistical stability can be obtained for along-beam spatial lags only. Also, along-beam lags can be treated with a Fast Fourier Transform (FFT), which greatly speeds the computation, and permits the use and benefits of windowing. Thus, for the quick analysis, wavenumber spectra along each beam are formed. No spatial correlations involving different beams are used. Finally, the frequency-wavenumber coefficients are squared to form power estimates. This helps to increase the robustness with respect to small heading variations, as experienced on *FLIP* (section 4d below), and further reduces the computational load.

b. Implementation

The HR sonar-derived velocity estimates from 78 to 225 m in slant range along each beam are used (50 estimates along each of four directions). A temporal FFT is performed on 256 samples in time (192 s) at each of these locations, using a $\cos^2$ window. In each frequency band, the data along each beam is spatially windowed with a $\cos^2$ window, zero-padded to 64 points, and a spatial FFT is performed. The results are squared and normalized to create velocity variance-density estimates on a grid of frequency versus along-beam wavenumber: $P(f, k_r)$, where $0 \le f < 1$ Hz and $-1/6) \le k_r \le 1/6$ cycles per meter (cpm). The temporal window is advanced 96 s (half the segment length), the procedure repeated, and the results are accumulated over seven consecutive time segments, resulting in net data spans of 4*192 s = 12.8 min. The power estimates versus frequency are averaged

with a 1-2-1 filter. Together with the windowing, this results in a net increase in the degrees of freedom for each estimate by a factor of 3. The frequency resolution is (1/192) Hz, and the wavenumber resolution (not counting zero padding) is (1/152) cpm. For each value of f and k_r, the linear dispersion relation yields a corresponding angle $\pm\theta$ between the sonar beam and the direction of propagation of a surface wave. Since only the range component of velocity is measured, the velocity variance densities are weighted by $\cos^2\theta$ (where θ is the angle between the sonar beam and surface wave). For angles nearing 90°, the along-beam component vanishes, leaving only noise. Over all spectral points where this angle would be real (i.e., where $k_r < k \equiv (2\pi f)^2/g$), the variance density estimates are weighted by an additional $\cos^2\theta = (k_r/k)^2$. The next spectral point in the k-wise direction outside the region where θ is real is also included, with a weight of 1.0, appropriate to $\theta = 0$. This helps account for windowing and small advective effects. The results are summed separately over positive and negative values of k_r. The additional weighting by $\cos^2\theta$ decreases the effects of noise, and suppresses harmonics present in the actual waveforms. Some additional adjustments are also performed, to account for the inherent range smoothing, spikes, velocity wrapping, and noise levels of the data; these will be discussed in section 4. Finally, dimensionless spectra (or "saturation spectra") are formed by multiplying the velocity-variance densities by $(2\pi f)^3 g^{-2}$. For examination of the directional distribution versus frequency and many other purposes, this is a useful form. The data from each sonar beam is thus reduced to two estimates at each frequency, corresponding to the two opposing directions along the beam. The results are eight directional estimates at each frequency: each has an angular weighting of $\cos^4(\theta-\theta_k)$ truncated at $|\theta-\theta_k| < \pi/2$, where the eight directions θ_k are spaced at 45° increments around *FLIP*'s average heading over the time period.

For a different number of sonar beams, the geometry of the beams and the analysis can be adjusted. For N beams, the beam spacing should be 180°/N (180° reversals are permitted), and the weighting should be adjusted to result in a net weighting of $\cos^N(\theta-\theta_k)$. This yields a good match between the weighting and the directional coverage.

Besides being quick, the technique described here reduces the need to correct for various weaknesses inherent to the data (to be discussed in more detail in section 4). For example, FLIP's heading could be incorporated at each moment; but then a simple FFT in time could not be used. The directional resolution commensurate with full use of the 400-m aperture of the array (2 km including the LR sonar) may make the effort worthwhile for certain purposes. However, the quick-analysis provides robust estimates of dominant frequencies and directions with short averaging times, and is useful for investigating directional wave evolution during rapidly changing conditions. It is also conceptually and computationally simple.

c. Circular Fourier components

The eight directional estimates at each frequency can be transformed into five circular Fourier components of the directional distribution, D_0 to D_4 (say), where

$$D_n(f) \equiv \pi^{-1/2} \int_{-\pi}^{+\pi} d(\theta,f)\, e^{in\theta}\, d\theta, \qquad (3.1)$$

with $d(\theta,f)$ defined as the directional distribution of wave energy at the frequency f. For example, the simple inverse problem of which values of D_0 through D_4 would give rise to the observed eight directional estimates can be solved. Equivalently, a simple 8-point FFT can be performed on the eight estimates, and the results corrected for smoothing by the $\cos^4$ weighting. Since the eight directional estimates weight the variance symmetrically about each of the eight directions, the odd (imaginary) part of the n=4 component is not estimated. In view of this, the last component D_4 (the "Nyquist component") is of limited use, and may be discarded. The zeroth component D_0, which is the total variance at frequency f, is real. Thus, the useful information is contained in just 7 real numbers per frequency band (or 1 real and 3 complex). By similar arguments, an N-beam sonar system would yield N circular Fourier components, using the analogous analysis (with evenly spaced beams).

The circular Fourier components are a useful form for the information, since they are easily rotated from FLIP's heading to a true North reference. For example, the results from short segments can be rotated and then averaged together over longer times, reducing degradation due to increased heading variability over longer timespans. The reliability of the directional estimates discussed here is limited by the statistical variability of the waves over finite averaging intervals in both space and time. The observed variability of the mean direction D_1 will be investigated below, and related to an estimate of the number of degrees of freedom. Discussion of the characteristics and stability of the higher components is deferred.

Note that the complex value D_1 provides exactly the information needed to calculate the net vector wave momentum at fixed frequency from the scalar E/c: the angle on the complex plane gives the vector direction of the net momentum, and the magnitude (between 0 and 1) accounts for the fact that momentum in oppositely directed waves partially cancels. For this purpose, the higher Fourier components cancel out. Here, the coordinate system is defined so that the angle of D_1 on the complex plane is the bearing of the net wave momentum on a true North compass: N is the positive real axis, and E is the positive imaginary. (This is right-handed if one is looking up from below).

d. Projection techniques

It is useful to project the results onto either a continuous analytic function of angle, or onto a dense array of angles. The simplest reconstruction in direction at each frequency is the inverse FFT of the circular components D_0 through D_3. This usually results in "negative-energy" regions. For display, the negative regions can be zeroed, or one can take the absolute values; this latter option allows the viewer to see the effect, yet permits plotting of log-density versus frequency and direction to capture the full dynamic range. For example, directional spectra were computed over 52-min segments every 2 h throughout SWAPP, with higher sampling rates over the initial hours of the year-day 63 and 67 wind events. A selection of directional spectra over the initial period of the day 63 wind event is shown in figure 5, using the inverse FFT reconstruction (with the $\log_{10}$ of the magnitudes of negative regions included). Even with this simplest reconstruction, much can be seen about the evolution of the directional wave field. A swell peak arose between about 0600 and 1000 UTC on year-day 63, about 6 h prior to the onset of strong winds (at 1530 UTC); also, note that early in the series the directional maximum rotates with frequency in one direction, while later on the directional maximum rotates the other way.

A desirable property of a projection technique is that the results be non-negative, since negative energies or momenta are unphysical. One approach is to fit the distribution to an analytic form such as $\cos^p(\theta/2)$. This form represents only two components, say D_0 and D_1. However, it can provide "predictions" of the higher moments, based on approximate consistence with this form. This will prove useful in setting error bounds on the directional estimates (section 5a), so the relationships are outlined below. Alternatively, one can solve for a non-negative directional distribution which would give rise to the measured circular Fourier components. For example, one could use an iterated maximum likelihood method, constrained to the smoothest possible solution (c.f., Herbers and Guza 1990). Such resolution enhancing methods do not increase the accuracy of the lowest circular moments; rather, they are employed to fill in details related to higher moments. Indeed, knowing just what level of detail to retain in the results is something of an art. Since the lowest few circular components are the main interest here, we defer further discussion.

The directional components for the functional form $\cos^p(\theta/2)$ are straightforward to evaluate. The mean component D_0 is expressed in terms of the gamma function (Abramowitz and Stegun 1965):

$$D_0 \equiv \pi^{-1/2} \int_{-\pi}^{\pi} \cos^p(\theta/2)\, d\theta = 2\pi^{1/2} \left\{ \frac{\Gamma(0.5(p+1))}{\Gamma(0.5(p+2))} \right\}. \quad (3.2)$$

In practice, it's useful to normalize the higher components by D_0 so that they are constrained to have magnitudes between 0 and 1. Then (3.2) yields the normalization factor, and the higher components (for n>0) become

$$D_n = \prod_{k=1}^{n} \frac{p-2(k-1)}{p+2k} \quad (3.3)$$

(Longuet-Higgins et al. 1963), where Π is the product symbol. From this, we find

$$p = \frac{2|D_1|}{1-|D_1|}. \quad (3.4)$$

This permits simple conversion from an observed value of D_1 to an equivalent $\cos^p(\theta/2)$ model. For a directional distribution in agreement with this model, the relationship between D_1 and all the higher circular components D_n would be set by (3.3) and (3.4).

4. Data quality concerns

We now consider some weaknesses of the Doppler sonar data, and how these might affect the results of the above analysis. Some details of the processing will also be clarified. The phenomena to be considered are: (1) geometric corrections for slant range versus horizontal range along the surface (including the vertical angle of the corresponding radial velocity estimate); (2) low coherence Doppler estimates; (3) velocity wrapping of the Doppler shift past $\pm\pi$; (4) corrections for the motion of *FLIP*; (5) horizontal advection by mean flow; (6) Range-dependent effects; (7) noise and filtering; and (8) importance of non-linear terms in describing the waves.

a. Geometric corrections

The geometry of a sonar beam is shown in Fig. 4. The range interval used in the following analysis is from 78 m slant range to 225 m (range bins 26–75, inclusive). As will be discussed below, the latter cutoff is selected to fall just short of a change in the probability distribution of surface velocities with range, thought to indicate the onset of shadowing effects. At 78-m slant range, from 35-m depth, the incident angle on the surface is 26.7° (neglecting refraction), and the corresponding horizontal range along the surface is 69.7 m. At 225-m slant range, the incident angle is 8.9°, and the horizontal range is 222 m. Thus, the net horizontal range interval is 152.3 m, and the incident angle upon the surface spans 17.8°.

For the quick analysis, the geometric effects are accounted for approximately by using a linear least-squares fit of the horizontal range and phase to regularly spaced slant range "bins." The use of a linear fit to account for the geometry permits the use of the FFT in range. Since there is a large volume of data to process,

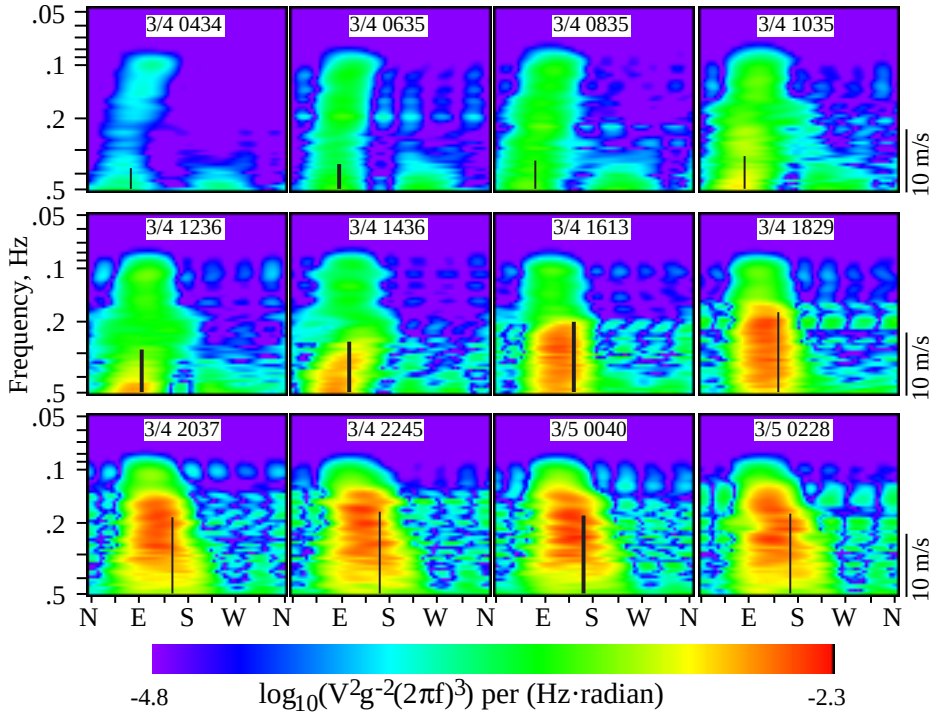

Fig. 5. A series of frequency-directional spectra, using the quick analysis. Displayed is the $\log_{10}$ of the spectral density (as a color) on a direction versus $\log_{10}$ frequency plane. The simplest reconstruction is used (inverse FFT), and negative sidelobes are included by taking the absolute value. All times are UTC. Black vertical lines represent windspeed and direction; magnitude scale on right.

this economy is important. The resulting distortion of the range-wise profile is small. The linear fit for horizontal range yields 3.1005 m per bin starting at -9.6077 m for range bin zero. The true horizontal interval of the data used in the analysis is 152.3 m, while the linear fit yields an apparent interval of 151.9 m.

Another effect is introduced by the variation in incident angle on the surface: the radial velocity (as measured) has a vertical component. For waves traveling parallel to the beam, the horizontal and vertical components are in quadrature, so this effectively introduces a phase-shift versus range in the measured wave component. The fit of incident angle over the range interval employed yields -0.3222 degrees per bin, starting at 31.001 degrees. The linear fit yields an apparent angle subtended of 15.8°, in contrast to the true angle of 17.8°. The net effect for waves propagating parallel to the beam is to produce a small "bias" in the estimated wavenumber of about 1/23 cycle over the total range interval of 152 m, or about 0.0003 cpm (an increase for waves traveling along the beam one way, a decrease for the other direction). Waves traveling perpendicular to the beam, on the other hand, are undetectable except for the small vertical component. Sensitivity to such perpendicular components is minimized in this quick analysis, due to the additional weighting by $\cos^2\theta$, so this effect is simply neglected.

Simulations, using the geometrically correct model to provide input "test waves" to the analysis, indicate that these approximations have negligible effect on the accuracy of the results, in either magnitude or direction.

b. Low coherences and velocity spiking

Estimates of the Doppler shift of the backscattered sound are formed from the phase of a measured covariance between the signal at one time and that at a later time (Pinkel and Smith 1992). Here, the time lag used is 0.8 milliseconds. On occasion, the signal can become uncorrelated within this short time. This is associated with suspected "breaking events" (or near-breaking events) in the surface wavefield (figure 6). The result is an unreliable phase estimate, and hence a spurious velocity, which often appears as a "spike." To remove these, the coherence levels are estimated (inversely related to the "bandwidth" estimates found in the literature; see, e.g., (Theriault 1986), and low values are replaced by linear interpolation from neighboring points. Since these occur mainly as isolated points, this approach is probably sufficient to subdue any cumulative effect.

c. Velocity wrapping

Another problem is "wrapping" of the phase of the coherence estimates past $\pm\pi$, due to the occurance of

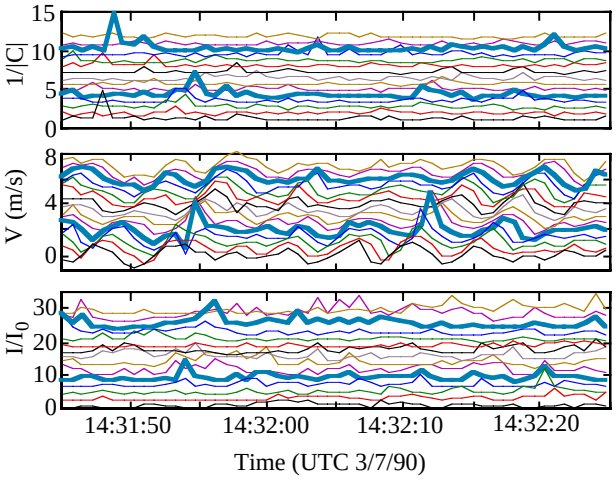

Figure 6. An example segment of coherence, velocity, and intensity data. Data are offset upwards for successive range bins; data from about 124 to 170 m range are plotted against time. For visual consistency, the inverse of coherence magnitude is plotted (top plot); values exceeding 4.5 ($20^{1/2}$) correspond to coherences below the 68% confidence level. The lower bold line traces a coherence event that appears to be related to spikes in both the velocity (middle plot) and intensity (bottom plot). Several other low coherence events are seen that have no corresponding effect on velocity or intensity; for example, along the upper bold line.

very large velocities. Since the velocity is estimated from the 2-component arctangent of the phase, this results in a large velocity estimate with the wrong sign appearing in the data. For the operating parameters of the HR system (195kHz center frequency and 0.8 ms lag), phases of $\pm\pi$ correspond to velocities of ± 2.37 m/s. This is sufficiently large to avoid wrapping in almost all the data except, on rare occasion, in estimates from near the crests of waves. In contrast to the above problem of low coherences, these "wrapping events" often occur in a sequence extending along the space-time trajectory of the crest (see figure 7). The result could have a perceptible effect on the estimated spectrum, if not properly accounted for.

At first glance, it would seem possible to unwrap the velocities with a simple difference threshold. For example, the range derivative of velocity is taken, "jumps" corresponding to more than π in phase are reversed, and then velocity is re-formed by integration. However, it is possible to have a large jump surrounded by two smaller return jumps of nearly equal size. In such a case, this simple approach yields "half-unwraps." These failures result in "Heaviside jumps" of 2π in velocity, or velocity jumps of almost 5 m/s, which are worse than the original defects.

To reduce the incidence of phase wrapping without introducing even more severe anomalies, an unwrapping scheme consisting of several passes was devised. First, for the beams aimed nearly parallel to the wind, the wrapping point is "biased" in favor of larger velocities in the downwind direction, rather than being located symmetrically at + and – π. The level of bias is based on observed skewness of the velocity distribution (figure 8). For example, in the case shown, the minimum probability density occurs near -2.0 m s^{-1}; however, because troughs are generally smoother than crests, it proves beneficial to bias the wrap point a little farther, placing it at -1.8 m/s. Next, a "large" finite difference threshold, 1.3π in phase, is used to search for up to three wrapped values in a row in range for each time sample; however, the points are not unwrapped unless a corresponding return jump is identified. In the third pass, a second-derivative criterion is applied, in which individual points are unwrapped if the jumps on both sides add up to more than 2π. This has to be done after the multi-point search, since

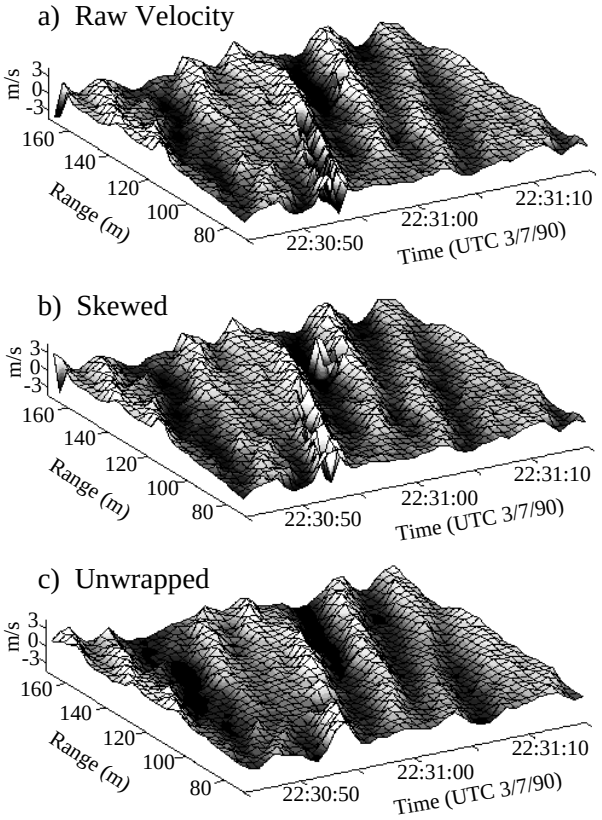

Figure 7. An example of velocity wrapping, showing how the wrapping may extend for several samples along the moving crest of a wave. Note the prominent "trough" where the crest of the second wave ought to be in the raw data (top plot). To reduce this effect requires several processing steps, starting with changing the "wrap point" to match the observed skewness of the velocity field, depending on direction relative to the wind (middle plot); note that the "false trough" is reduced, but a "false peak" now appears in the following wave trough. Then several passes are made, using a variety of "jump criteria" to unwrap the velocities (see text). The final result is shown in the lowest panel. The crest of the second wave still appears somewhat damaged, but is greatly improved (This segment is one of the worst cases encountered.)

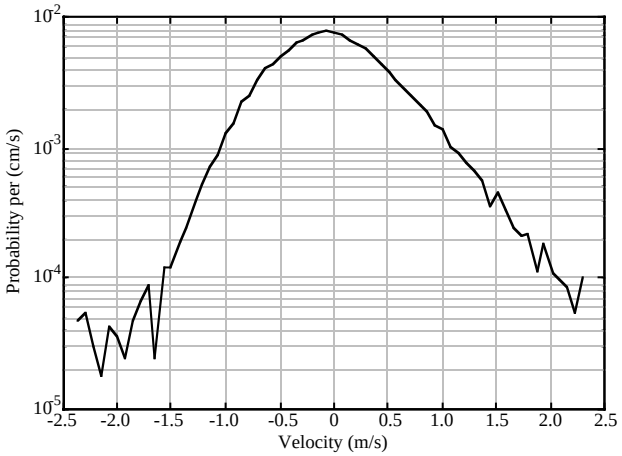

Figure 8. Log_{10}(pdf) of "raw velocity," from the same segment of data as shown in figure 7, top plot. The least likely values lie near –2.0 m/s for this (downwind directed) beam, rather than at the symmetric value corresponding to $\pm\pi$ (±2.37 m/s). It is beneficial to unwrap about -1.8 m/s in this case, rather than about the true minimum. This is because the wave troughs are smoother, making artificial discontinuities easier to detect.

there can be a single unwrapped value in the midst of a row of wrapped values. Finally, remaining outliers are deemed to be "spikes" and are replaced by block averages including all immediate neighbors (9 points). Out of 153,600 points in the "worst case" segment used for illustration here, 22 were identified as wrapped (0.014%), and 622 were identified as outliers and hence smoothed (0.4%). All identified points were in beam 4 (of 4 beams), which was aimed most nearly downwind.

With the repeat-sequence coding, the accuracy of the velocity estimate is related to the lag at which it is computed. Thus, there is a trade-off between the accuracy of the velocity estimates at good points versus the number of spikes and wrapped points. Here, although the wrapping is enough of a problem to discuss in some detail, it occurs in less than 0.015% of the data even in the "worst case" segment. Thus the covariance lag employed appears to be a good choice.

Judging from the illustration segment, it is not easy to devise an unwrapping scheme which unwraps all the "right" points but no others (indeed, even using the sophisticated pattern recognition techniques associated with the phrase "by eye," disagreements can arise on the status of a particular point). However, the scheme described here appears to correct all but a few isolated points; this should restrict the effects to a negligible increase in the white noise level of the spectrum.

d. Motion of FLIP

The motions of *FLIP* which significantly affect the surface wave measurements are 1) variations in heading over the time interval of data from which a spectral estimate is to be formed, and 2) the velocity of the sonar transducers at the times of each transmission and measurement.

The heading variations of *FLIP* over a 3-min time interval (roughly the shortest usable interval) were generally less than 3° rms, depending on the weather (up to 4° in the strongest winds, less in light conditions). At 220-m range, ±3° corresponds to ±12 m. A 24 m wavelength corresponds to 4-s period surface waves, so these variations may be important at the highest measured frequencies. In the quick analysis, the $\cos^4\theta$ directional weighting restricts influence to waves traveling within about 22.5° of the sonar beam direction. For a wave propagating 22.5° off the beam direction, a cycle in 24 m along the direction perpendicular to the beam corresponds to a true wavelength of 9 m, or a wave period of about 2.4 s. Thus, the effect is reduced, and restricted to yet higher frequencies. The quick analysis further reduces sensitivity to the induced phase variability by using sums over the squared magnitudes of the coefficients. By using a restricted range interval, using only spatial lags along individual beams, and summing squared magnitudes of the time-space Fourier coefficients, the effect of heading variations on the estimated directional frequency spectrum is reduced. Simulations indicate that the effects of the small heading variations are reduced to smoothing the spectral densities slightly in both direction and frequency. These effects are neglected. However, it should be noted that the heading variability affects the results in a way that depends on the frequency (wavenumber) of the waves, as noted above, so caution should be exercised in interpreting, for example, spectral slope versus frequency at the high end, that is for periods less than 3 or 4 s.

Wave-coherent transducer velocities, due to motion of the platform, are accounted for by removing a mean velocity formed over the relevant range interval from the data of each beam, for each ping. For waves much shorter than 152 m, this has little effect. For waves much longer than 152 m, the estimate is essentially based on the trend and curvature of the velocity profile over the 152 m aperture of each beam. (For reference, 10-s waves have wavelengths of about 155 m). The performance for such long waves was simulated, and it is seen that the amplitude of the response varies from 0.0 for very long waves to 1.0 for short ones (Figure 9). To correct for this, the amplitudes at each frequency are divided by the reference profile (Figure 9), which is averaged over all beams and all wave directions. To prevent singularities at the low frequencies, the reference response is first thresholded above 0.2 (i.e., values below 0.2, corresponding to frequencies below 0.07 Hz, are set to 0.2). In the comparison with the wave wire derived power spectra (discussed below), this is found to result in good agreement for waves with periods up to 14 s.

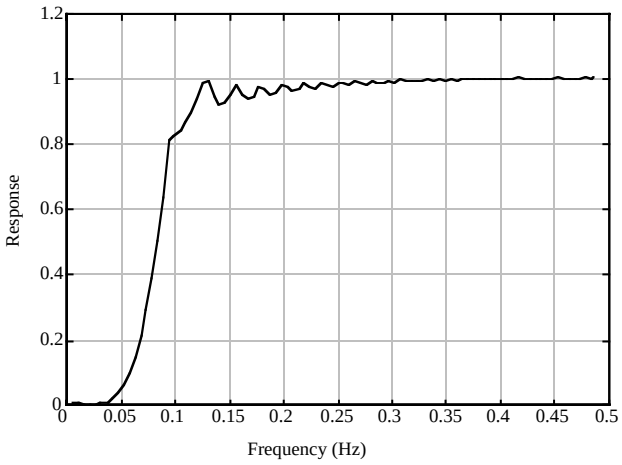

Figure 9. The computed response versus surface wave frequency in forming the eight directional estimates from finite Fourier transforms with range-means removed. The response is an average over all beams, all possible wave directions. The corresponding wavenumber is obtained from the linear dispersion relation.

e. Horizontal advection

A uniform horizontal flow past the platform alters the effective dispersion relation of the waves. It makes the wavenumber associated with a given (encounter) frequency into a function of direction. In terms of the wavenumber component along a given beam at a fixed frequency, both the maximum possible value and the direction associated with it can be altered. The quick analysis makes use of the estimated angle between a given beam and a wave component, based on the arccosine of the ratio of the measured component along the beam "k_b" and the magnitude k from linear dispersion. The following explores how much error is introduced by ignoring the mean flow.

In the absence of a current, the linear dispersion relation for gravity waves is simply $\omega^2 = gk$, where ω is radian frequency, k is the magnitude of the wavenumber **k**, and g is gravity. With a uniform current **U**, this becomes:

$$\omega^2 = gk + \mathbf{U}\cdot\mathbf{k}. \tag{4.1}$$

Defining θ_k as the angle between the sonar beam and **k**, θ_u as the angle between the beam and **U**, and U as the magnitude of **U**, this may be rearranged to obtain k in terms of ω:

$$k^{1/2} = \frac{2\omega g^{-1/2}}{1+(1+4U\omega g^{-1}\cos(\theta_k-\theta_u))^{1/2}} \tag{4.2}$$

The form (4.2) is chosen as it is well behaved for $U \to 0$. For a 3-s wave, $c_o \equiv g\ \omega^{-1} \approx 4.7$ m s^{-1}, while the mean flow past *FLIP* is rarely more than 0.15 m s^{-1}. Thus it is reasonable to make the assumption that $\hat{U} \equiv U\omega g^{-1} \ll 1$. Then a reasonable approximation to (4.2) is:

$$k \approx \frac{k_o}{1+ 2\hat{U}\cos(\theta_k-\theta_u)} \tag{4.3}$$

where $k_o \equiv \omega^2 g^{-1}$ is the "uncorrected wavenumber." For example, for $\hat{U} = 0.03$ (as for the 3 s wave with 0.15 m s^{-1} current), we find from (4.3) about 0.943 times k_o, while the actual value should be 0.944 [from (4.2)]. For longer waves, or weaker flows, the error is even smaller. The approximation (4.3) is quite good and can be used to estimate the effect on the quick analysis.

It is the along-beam component of the wavenumber that is relevant to the quick analysis:

$$k_b = k\cos\theta_k \approx \frac{k_o\cos\theta_k}{1+2\hat{U}\cos(\theta_k-\theta_u)}. \tag{4.4}$$

With an arbitrary mean flow, the maximum measured wavenumber component along the beam at fixed apparent frequency may not be associated with a wave exactly parallel to the beam. The angle associated with the maximum measured component k_b is found by examining the derivative with respect to angle:

$$\frac{\partial k_b}{\partial\theta_k} \approx -k_o\frac{2U\omega g^{-1}\sin\theta_u + \sin\theta_k}{(1 + 2\hat{U}\cos(\theta_k-\theta_u))^2}. \tag{4.5}$$

Setting this to zero, the maximum is found at

$$\sin\theta_{kmax} \approx -2\hat{U}\sin\theta_u. \tag{4.6}$$

Only the component of current orthogonal to the beam affects the direction, and the maximum detected wavenumber component corresponds to a wave biased slightly into the current. For $\hat{U} = 0.03$ directed at 90° to the beam, the maximum k_b would be turned 3.4° into the current from the sonar beam's nominal direction. The net direction of the weighted estimate would be turned by about half this amount, since part of the $\cos^4\theta$ weighting is effected by the component of velocity detected, and only part corresponds to this analyzed angle: one would obtain a weighting by roughly $\cos^2\theta\cos^2(\theta\pm\theta_{\mathrm{kmax}})$. Also, the oppositely directed estimate is turned in the opposite direction (again into the current), so the net effect on the estimated mean direction of the waves, in particular, is even smaller.

Now the corresponding maximum magnitude of k_b is estimated. First note that, to the same order of accuracy in $\hat{U}$ as (4.3),

$$\cos\theta_{kmax} = (1 - \sin^2\theta_{kmax})^{1/2}$$
$$= (1-4\hat{U}^2\sin^2\theta_u)^{1/2} \approx 1. \tag{4.7}$$

Next, expand $\cos(\theta_k-\theta_u) = \cos\theta_k\cos\theta_u + \sin\theta_k\sin\theta_u$, and again neglect the term of order $\hat{U}^2$. At this order of approximation, we find

$$k_{bmax} \approx \frac{k_o}{1+2\hat{U}\cos\theta_u}. \tag{4.8}$$

In other words, at this order of approximation, only the component of flow along the beam affects the magnitude of the maximum wavenumber component detected by the beam, and only the component orthogonal to the beam affects its direction. Again using $\hat{U} = 0.03$ as an example, this could lead to a maximum k_b as much as 6% different from k_o.

These effects, while small, are relevant to many real-world measurements of the directional spectrum of waves (those which make use of a wavenumber based on frequency). A convenient aspect of the Doppler sonar data is that the mean flow is easily estimated from the same data, and can be taken into account. At the lowest order in the nondimensional current, one need only adjust the scaling of $\cos^2\theta = (k_r/k_{bmax})^2$ used in the additional weighting factor [using the parallel component of flow in (4.8)], and include a small turning angle due to the orthogonal component [from (4.6)] in the inverse problem of estimating the circular Fourier coefficients, now from slightly irregularly spaced data. Since the quick analysis allows for some error in the wavenumber magnitude estimate, by including an extra coefficient in the wavenumber direction, the effects on the directional estimates derived here are small enough to neglect (for the data shown here); thus, this correction is not applied.

f. Range dependent effects

The acoustic pulses impinge on the surface at an angle which varies with range from the instrument. Because of this, it is reasonable to expect the characteristics of the measurements to vary with range. To explore how this affects the velocity estimates, histograms were made of the distribution of velocities versus range (figure 10). The distribution of velocities becomes narrower beyond 225-m slant-range. This distance corresponds to an incident angle of about 9° on the surface. The change in velocity distribution could be the result of shadowing of extreme velocities sometimes found at the crests of steep waves (cf., sections 4b and 4c), for angles shallower than the 9° corresponding to 225-m range. Alternatively, or additionally, very dense bubble clouds could cause the effective measurement depth to increase with range: as the angle of incidence gets shallower, sound penetrating the same distance through the bubbles before being attenuated does not get as close to the surface. Balancing the variations in velocity distributions with range against the desire to have a large aperture, the quick analysis described above makes use of velocities from about 78– to 225-m slant range.

Another range-dependent effect shows up in time-averaged velocities (not shown here). For a sonar beam aimed downwind, it is often observed that the mean downwind directed flow registers more strongly at near range than at far range. The effect is stronger than, and of opposite sign to, the effect of sensing only the component of flow parallel to the beam: at near range, the vertical incidence angle is higher, so the component of a horizontal downwind flow parallel to the beam would be reduced, rather than enhanced. The range dependence of the mean velocity measurement also appears to increase with increasing wind speed. A plausible hypothesis is that, at the nearer ranges, the acoustic beam penetrates farther into the bubble layer, effectively measuring a velocity nearer the surface in the strongly sheared downwind flow. This is consistent with the above interpretation of the changes in the wave-related velocities: the farther range measurements correspond to motion at slightly greater depths. While it is conceivable that this could permit estimation of the near-surface shear, the characteristics of the bubble layer are too poorly known. If this hypothesis is correct, the net effect on the quick analysis is negligible.

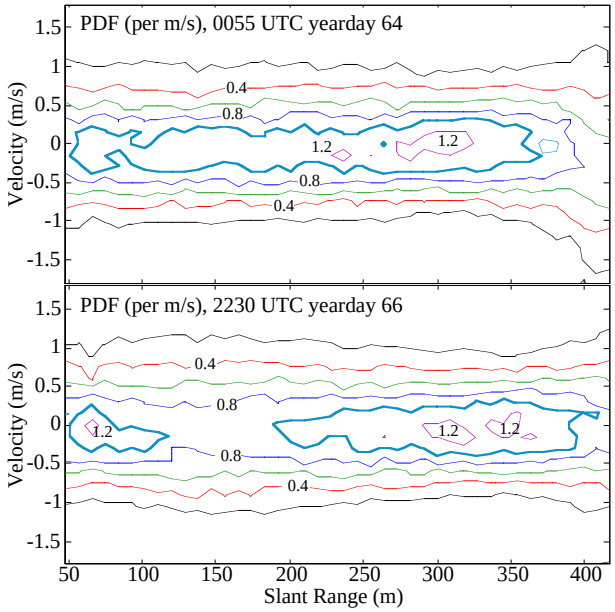

Figure 10. Histograms of velocity at various ranges, for two representative time periods. Contour interval is 0.2; normalization is such that the integral over all possible velocities in m/s is 1.0. The response versus range can be broken into four regions: (1) From 50 to 80 meters or so, both the beam pattern and incident angle vary markedly, causing the distributions to vary (the sonar is at 35 m mean depth). (2) From 80 to 225 m or so, the distributions are wider (so the peak density is reduced), probably reflecting more accurately the distribution of horizontal velocities near the surface (3) From 225 to 360 m or so, the distributions are somewhat narrower, consistent with a slightly greater effective measurement depth (due to "shadowing" of the peaks at the lower grazing angles, or increased absorption near the surface due to bubbles). This suppresses some higher-wavenumber activity, resulting in a narrower distribution of velocities. (4) Beyond 360 m, noise becomes important, resulting in progressively flatter distributions.

g. Noise and Filtering

The noise characteristics arising from the ping-to-ping incoherent Doppler estimation scheme were ex-

plored in both theory and experiment by Pinkel and Smith (1992). The noise in the Doppler estimates is slightly correlated from one sample to the next. For the particular operating parameters used during SWAPP, the noise correlation-squared in adjacent range samples (i.e., the fraction of variance shared) is about $(1/13)^2$. To evaluate the predicted noise level, this model noise covariance is Fourier transformed and the magnitudes squared, and the result is scaled by the observed level of noise per sample of 12 cm/s RMS. The resulting estimates of the spectral noise levels are subtracted from the squared time-range transforms of the measurements, used in the quick analysis, before weighting and summing separately over opposite directions.

The signal also is correlated from sample to sample. The spatially distributed "true velocities" are sampled with a roughly triangular-shaped weighting in range, in which adjacent samples overlap. For the highest-frequency waves, which are limited by the spatial resolution, it is helpful to correct the range-wise transforms for this smoothing. Rather than use the $\mathrm{sinc}^4 k$ shape arising analytically from the approximate triangular shape of the weighting, the more accurate digital sampling approach of Pinkel and Smith [1992] is evaluated and transformed to k space. This correction is also applied before the sums over k. No correction is applied for the effects of averaging of the signal in the cross-beam directions. These adjustments have minor effects on the results.

h. Non-linear terms

In general, surface gravity waves are not perfectly sinusoidal, so harmonics are present. The second harmonic has both twice the frequency and twice the wavenumber of the primary wave. In contrast, a free wave (primary harmonic) with twice the frequency would have four times the wavenumber. In the context of the quick analysis, the harmonic of a lower frequency wave has a wavenumber just half as large as that for the free wave propogating in the same direction. In the quick analysis, the components are weighted by an additional $\cos^2\hat{\theta} \equiv (k/k_o)^2$, where k_o is the free wavenumber magnitude from linear dispersion. Thus, the harmonic of the longer wave is suppressed by a factor of 1/4 in velocity variance, relative to a free wave propogating in the same direction. The implication is that the energy content in such harmonics is reduced in the quick directional analysis of the sonar data.

5. Error Estimates and Comparisons

a. Stability of the Directional Estimates

An attraction of the quick analysis is the promise to provide directional wave estimates with good temporal resolution, over extended periods of time. How stable are these directional estimates from a given time interval of data? Here, an answer is first attempted through an empirical approach, assuming that the true evolution of the directional wavefield (e.g., as would be found from a much larger sample area) is smooth in time. These empirical results are then compared to estimates based on the observed directional distribution and a guess at the number of degrees of freedom brought to bear in the application of the method.

To address this, directions of the first circular Fourier components (D_1 in the above terminology) are examined as functions of time. The magnitude and direction of this component correspond to a conversion vector needed to translate wave energy into the vector momentum of the waves, as mentioned above; thus it is of physical interest. For this study, two time segments were selected, in which continual "wave-mode" measurements were taken, and the direction of the wind and waves varied smoothly in time (figure 11). The first segment (yearday 63) is characterized by an approximately constant turning rate, whereas the second (yeaday 67) has fairly constant wave direction. The first segment consists of 31 segments of 12.8 min each, and the second consists of 75.

To estimate directional uncertainty, various order polynomials are fit in time in a least-squares sense, and the residual variances are examined (figure 12). The residual variances are calculated by (1) subtracting the polynomial fit, (2) squaring and summing the results, and (3) dividing by (M-P-1), where M is the number

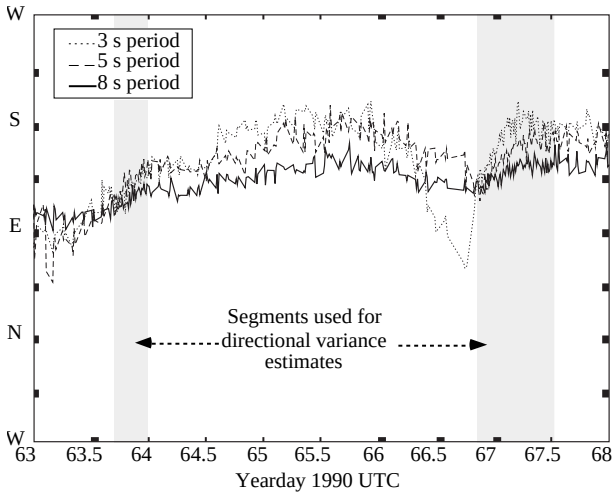

Figure 11. Direction versus time from "D_1" (see text), showing the two intensive time periods selected to evaluate the variance of the directional estimate. The first (day 64) is just over 6 hours long, beginning a few hours after the onset of strong winds. The second segment is almost 11 hours long, again beginning several hours after the onset of strong winds. The segments are chosen for both continual "wave-mode" recording and for smooth changes in direction versus time; hence the beginnings of wind events are avoided. Away from these two intensive periods, the "one hour on, one hour off" structure of the data stream can be seen.

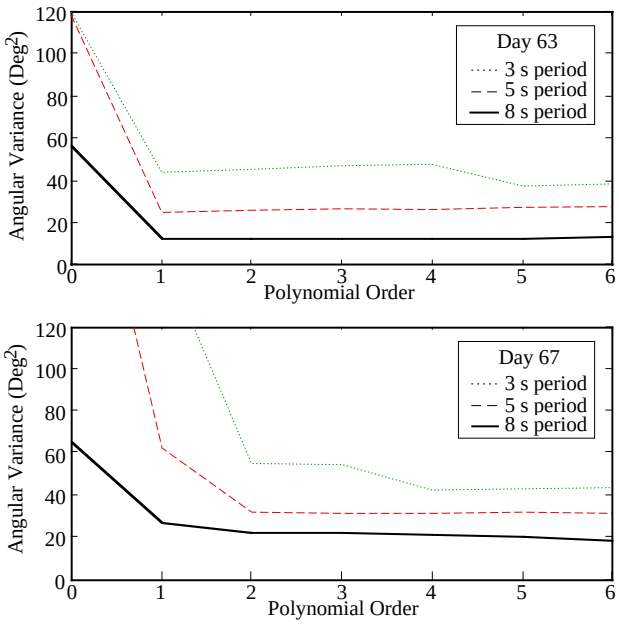

Figure 12. The residual angular variance after removing various order polynomial fits in time for the two intensive sonar periods (on yeardays 63 and 67). In general, a quadratic fit is sufficient to get a stable estimate of the angular variance.

of samples in time and P is the order of the polynomial removed (one more than P is subtracted to account for the mean, which corresponds to an order 0 polynomial). The estimates of the residuals are satisfactorily stable with respect to changing the order of polynomial removed, indicating that a quadratic fit is sufficient to describe the "smooth" variations in time. In other words, there is support for the initial assumption that the timescales associated with bulk changes in the wave field are long compared to the timescales of the random fluctuations due to sample error.

Next we compare these empirical results with estimates of the statistical variability one should expect, given the measured directional spread of the waves and the number of degrees of freedom. An estimate of the variance in D_1 orthogonal to its mean direction can be obtained directly from D_2, or indirectly (with an assumption about the "shape" of the directional profile) from D_1. Setting $\theta \equiv 0$ along the mean direction of D_1, so that $|D_1| = D_1$ (without loss of generality), we obtain

$$\sigma_\perp^2 \equiv \oint d(\theta)\sin^2\theta\, d\theta = \tfrac{1}{2}\oint d(\theta)(1-\cos 2\theta)\, d\theta = \tfrac{1}{2}\left(1-\mathrm{Re}\{D_2\}\right). \tag{5.1}$$

where $d(\theta, f)$ is (again) the directional distribution at frequency f. For the present purpose, D_2 can be adequately estimated from D_1 by assuming that the measured distribution is roughly in accord with the form $\cos^p(\theta/2)$ (c.f., Longuet-Higgins, et al. 1963). Then, using 3.4.3 and 3.4.2 to derive D_2 from D_1 (within 10 or 20%), we obtain

$$\sigma_\perp^2 \approx \frac{1-D_1^2}{2-D_1}. \tag{5.2}$$

The net angular uncertainty of D_1 is then

$$\sigma_\theta^2 = \mathrm{atan}^2\left(\frac{\sigma_\perp}{N^{1/2}D_1}\right) \approx \left(\frac{\sigma_\perp^2}{ND_1^2}\right) \approx \frac{1-D_1^2}{ND_1^2(2-D_1)} \tag{5.3}$$

where N is the (as yet unspecified) number of degrees of freedom. This allows an estimate of the angular uncertainty of D_1 without having to use the next higher (and presumably less stable) component D_2.

The effective number of degrees of freedom is the hardest part to estimate. First, the time-series of components D_1 used above comes from averages over a total timespan of 12.8 min, corresponding to 4 segments of 192 seconds each. Second, the coefficients are effectively averaged over 3 adjacent values in frequency, yielding $4 \times 3 = 12$ degrees of freedom so far. Third, there are two peices of information (real and imaginary parts) for each frequency, doubling the degrees of freedom (24 so far). Thus far, the count of degrees of freedom applies to estimates from the wire array as well. Fourth, a pair of beams is sufficient to estimate D_1, and two pairs of beams are used; to the extent that the information from each pair is independent, this can increase the degrees of freedom by a factor of up to 2, yielding 48 (maximum). Fifth, we estimate how many independent "samples" there are in the 152 m range interval used along each sonar beam. With a fixed $\Delta f = 1/192\ \mathrm{s}^{-1}$, we obtain from the linear dispersion relation

$$\Delta k = \frac{(2\pi)^2}{g} 2 f \Delta f = \frac{8\pi^2}{g(192s)T}, \tag{5.4}$$

where T is the wave period. Using this, the additional degrees of freedom due to the spatial extent of the array are estimated as:

$$1 + \Delta k(152m) \approx 1 + \frac{6.4s}{T}. \tag{5.5}$$

Finally, describing the variance and direction of the waves requires 3 numbers, so we subtract 2 from the total to estimate the net degrees of freedom. For the 4-beam sonar analysis, we obtain

$$N_4 \approx 48\left(1+\frac{6.4s}{T}\right) - 2 \tag{5.6}$$

(which may be high by as much as a factor of 2 for well aligned waves). In contrast, the analysis using just two beams would yield

Table 1. Observed and estimated angular variances of D_1 for yearday 63

Wave Period	3 sec		5 sec		8 sec	
#beams	4	2	4	2	4	2
$N_{est.}$	148.4	73.2	107.4	52.7	84.4	41.2
$\|D_1\|$	0.637	=	0.758	=	0.769	=
$\sigma^2_{est.}$	23.8	48.2	18.2	37.1	21.8	44.7
σ^2_{obs}	45.7	57.8	25.6	45.2	12.6	32.3
$\sigma^2_{est}/\sigma^2_{obs}$	0.52	0.83	0.71	0.82	1.73	1.38
σ^2_2/σ^2_4	1.26		1.77		2.56	

Table 2. Observed and estimated angular variances of D_1 for yearday 67

Wave Period	3 sec		5 sec		8 sec	
#beams	4	2	4	2	4	2
$N_{est.}$	148.4	73.2	107.4	52.7	84.4	41.2
$\|D_1\|$	0.590	=	0.692	=	0.762	=
$\sigma^2_{est.}$	29.4	59.6	25.4	51.8	22.7	46.5
σ^2_{obs}	54.7	71.5	31.8	57.6	21.7	52.9
$\sigma^2_{est}/\sigma^2_{obs}$	0.54	0.83	0.80	0.90	1.05	0.88
σ^2_2/σ^2_4	1.31		1.81		2.44	

$$N_2 \approx 24\left(1+\frac{6.4s}{T}\right)-2, \qquad (5.7)$$

and the equivalent tilt-and-roll analysis has $N_w \approx 22$ degrees of freedom for all wave periods.

Tables 1 and 2 show the observed sonar performance and error estimates for the 4 beam and 2 beam analyses, as described above, for data from yeardays 63 and 67, respectively. Values derived from a quadratic fit in time are used for all "observed" error estimates. The tables show observed and estimated directional errors at three selected wave periods: 3, 5, and 8 seconds. The wave periods are chosen to reveal trends in the results over the frequency range of interest. Of note are the ratios of estimated to observed directional errors (second to last row), and the ratios of the observed errors using 4 versus 2 beams' worth of data (last row).

Based on the above error analysis, the ratios of estimated to observed directional variances are expected to lie near 1.0 for the 2-beam case, and between 0.5 and 1.0 for the 4-beam case, depending on the degree of collinearity (i.e., on how close to 1.0 the magnitude of D_1 is). However, Tables 1 and 2 show two trends contradicting this. First, the ratio of expected over observed directional error increases with wave period for both 2- and 4-beam cases, in spite of the fact that the directional spread (as deduced from the magnitude of D_1) decreases with period. Second, the ratios of 2-beam over 4-beam variances (shown in the last rows of Tables 1 and 2) also increase with increasing wave period. Values of estimated over observed error variances exceeding 1.0 are possible, due to the fact that the magnitude of D_1 may be underestimated; however, we do not have an explanation for the relative performance of the 4-beam versus 2-beam analyses, nor for the observed trends with wave period. The increased performance of 4-beam versus 2-beam results is consistent between the two test periods, with the 4-beam performance exceeding twice that of 2-beams in both cases for 8 second waves.

b. Comparison with results from wire data

During SWAPP, three impedance wires were deployed on a boom about 18 m out from FLIP. These provided surface elevation records nearly continuously over the 20 days or so of the experiment, and slope measurements over the last 7 days, beginning at yearday 70.8 (there were some technical difficulties with one wire). It is of interest to compare results from the wire versus sonar data for both the variance and directions of the surface waves.

The first concern is how well the 1D spectra agree. To simplify this comparison, the wire data were finite-differenced in time to provide esimates of the vertical velocity spectrum (the raw data were sampled at 10 Hz). An example 1D spectrum of equivalent vertical velocity is shown in Fig. 13, from wire and sonar data taken on yearday 75 (16 March). The time of the spectrum shown here coincides with an overflight by an airplane carrying an interferometric SAR (synthetic aperture radar). Comparison with the SAR analysis is the subject of another paper (Goldstein et al. 1994). In this spectrum, there are two distinct peaks, one at

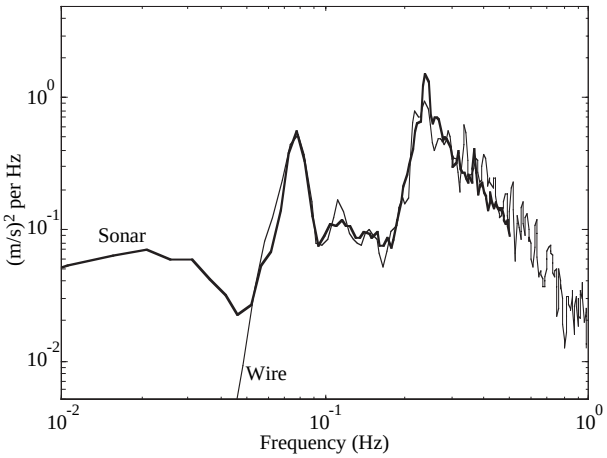

Fig. 13.Comparison of resistance-wire-derived vertical velocity spectrum (thin line) with that from the sonar "quick analysis" (thick line). The wind peak (near 0.2 Hz) was nearly at right angles to the swell (below 0.1 Hz) in this instance (2100 UTC year-day 75 1990).

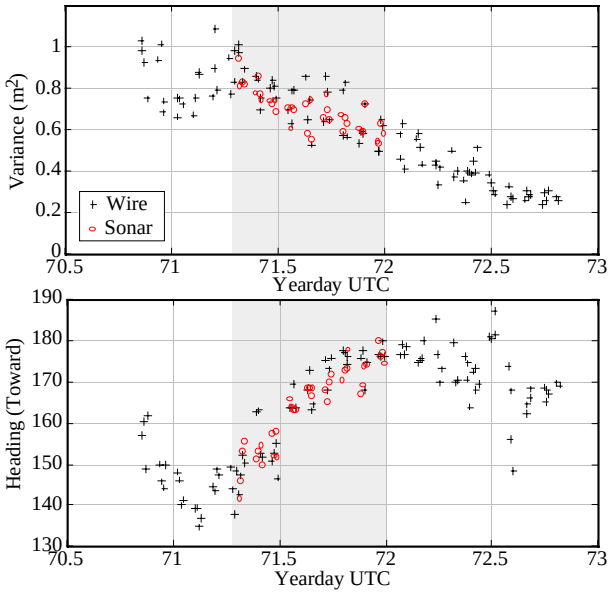

Figure 14. The elevation variance and high-frequency average direction surrounding the time segment chosen for the sonar-wire comparison. The high-frequency average is formed over 0.24 to 0.42 Hz (waves with periods of 2.4 to 4.0 s).

a "swell frequency" corresponding to a 13 s period, and the other corresponding to roughly 4 s "seas." These swell and sea peaks were separated in direction by about 100° in bearing. Several other time periods have also been compared, with similar agreement. With the processing outlined above, the correspondence between the directionally integrated sonar spectrum and the wire-derived spectrum is quite good for wave frequencies between about 0.07 Hz (14 s period) and a little under 0.5 (2 s period). The lower frequency limit is set by an apparent requirement to have at least a half-wavelength over the 152 m range interval used and from which the mean is removed in the sonar analysis. The high frequency limit is set by the range resolution of about 3 m, corresponding to a 6 m Nyquist wavelength (2 s period).

The other concern is how well the directions from the two data sets correspond. Since the third wire became operational at about yearday 70.8, later than the two intensive periods described above, a third time segment is employed. Figure 14 shows the wave variance and directions surrounding the selected segment, together with sonar-derived estimates within the segment. From year-day 71.3 to 72.0, there were nine 52-min runs in which the timing of the two systems gathering sonar and wire data were well-coordinated, spanning a total time of about 18 h. Each 52-min run yields four independent 12.8-min estimates, so the comparison is based on 36 samples. Over the whole time segment, the directions of the waves vary by about 40°, so there is no difficulty in tracking the directions unambiguously in both data sets. The mean differences in directions over this time segment are shown versus frequency in figure 15. There does not appear to be significant bias in the directions derived from the sonar versus wire data.

The directional analysis of the wire data follows as closely as possible that of the sonar data. The raw wire data were sampled 10 times per second. These were filtered and decimated to 2 samples per second. The elevation time-series from the three wires were then converted into one elevation and two tilt components, using the measured geometry of the wire array (a triangle approximately 1 m on a side). Time segments of 192 s were employed, with $\cos^2$ windowing and sliding averages of the various cross-spectral coefficients formed over total durations of 12.8 minutes (the non-power of 2 segment length poses no problem for this relatively small data set). A 1-2-1 filter was applied in the frequency direction to the results. Finally, the elevation-slope correlations are transformed into the first directional moment, following Longuet-Higgins et al (1963).

There are two choices in dealing with the small heading variations of the platform: (1) the heading can be used to rotate the slopes to a true North basis at the 2 Hz input rate, or (2) the mean heading over the 12.8 minute segment can be applied. The RMS difference in the resulting wave directions over the 18 hour test segment is less than 0.25°. That this is small is encouraging, since the sonar estimates rely on the mean correction. In the following error analysis, wire results using the first option (point-by-point correction) are used. No corrections were applied for the tilting of FLIP, and the corresponding motions of the boom supporting the wires.

To assess directional error levels, we employ the same technique as in section 5a: we remove successively higher-order polynomials fit to the estimated direction versus time, and examine the residual variances (Figure 16). A 2nd order polynomial fit in time is again sufficient to obtain stable results. The results and statistical error estimates are summarized in Table 3 for the wire versus sonar data. Comparing the estimated degrees of freedom for the wires versus sonar, we expect

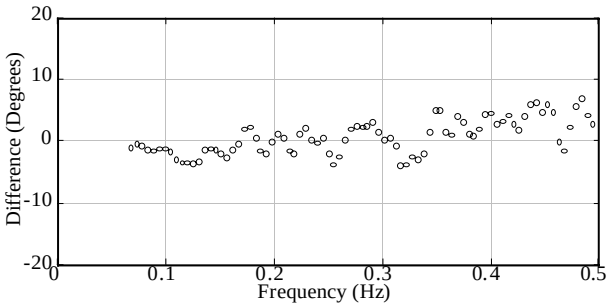

Figure 15. Time averaged difference in wave component direction versus frequency over the comparison segment. There does not appear to be a significant bias.

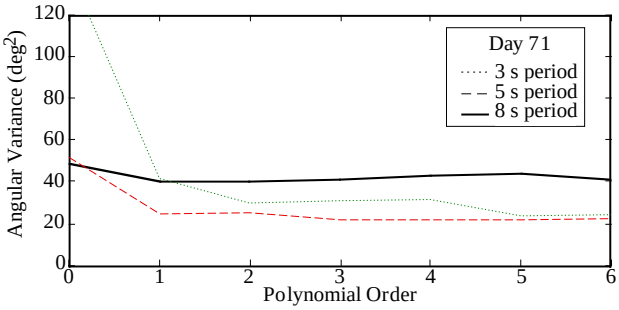

Figure 16. Residual angular variance versus order of the removed polynomial, for the sonar-wire comparison interval (using the sonar directions). Again, a second order polynomial is sufficient to provide stable results. The wire fits look similar (but with more variance).

Table 3. Angular variances of D_1 from sonar versus wire data, yearday 71

Wave Period	3 sec		5 sec		8 sec	
	sonar	wires	sonar	wires	sonar	wires
$N_{est.}$	148.4	22	107.4	22	84.4	22
$\|D_1\|$	0.575	0.606	0.660	0.711	0.758	0.781
$\sigma^2_{est.}$	31.4	184.4	29.5	113.2	23.2	78.3
σ^2_{obs}	30.1	166.0	25.8	189.5	40.8	40.3
$\sigma^2_{est}/\sigma^2_{obs}$	1.04	1.11	1.14	0.60	0.57	1.94
σ^2_w/σ^2_s	5.51		7.34		0.99	

the directions from the wires to yield up to 7, 5, and 4 times as much directional variance as from the four-beam sonar for 3, 5, and 8 s period waves, respectively. The observed ratios of wire to sonar variances (last row of Table 3) are 5.5, 7.3, and 1.0. The overall performance of the sonar is roughly in line with the expected improvement over the wire array, but the details vary, in particular with respect to the trend with wave period (as before). We again have an error estimate nearly two times smaller than the statistical expectation for 8-s waves, this time in the wire-derived values. In contrast to the earlier two segments, the observed sonar performance for this case is only about half as good as the expectation, putting it equal to the observed wire performance. It is plausible that these factors of two are spurious effects of the (finite sample) error analysis itself.

The expected directional error level depends on the directional spread, which is also a measured quantity. Here, the spread is estimated from $|D_1|$, resulting in (5.2). Thus it is of interest to compare the magnitudes of the D_1 coefficients from the two data sets, as well as their directions. Figure 17 shows wire-based and sonar-based values of $|D_1|$ versus time at two fixed frequencies, and time-averaged values versus frequency. The timeseries show that the wire-based estimates are much more variable than the sonar-based ones, for both the 3- and 8-s period waves. On the other hand, the frequency plot shows that the sonar-based values are biased to lower values, relative to the wire-based values. This bias increases at both the high- and low-frequency ends. At the low frequency end, the low bias of the sonar data is probably due to the effects of removing a range-mean velocity over 152-m intervals. At the high frequency end, as we approach the Nyquist wavenumber (6-m wavelength, or 2-s period), the direction becomes ambiguous, so we again obtain artificially broad distributions. In the intermediate frequency range, corresponding to wave periods of 3–12 s, the values are quite close, but with the sonar values consistently lower. An effect of bias toward low values would be to artificially increase the error estimate from (5.2).

It is hard to gauge how stable these error comparisons are. The error estimates are themselves subject to considerable error. The overall patterns seen in Tables 1–3 suggest that these error estimates are good to within a factor of 2 or so. There is a consistent overall pattern indicating that the four-beam analysis outperforms both the two-beam and wire analyses. The two-beam to four-beam performance ratios increase from about 1.3 to over 2 as wave period increases from 3 to 8 s. The wire to four-beam sonar performance ratios are more erratic, but average over 4, for 3–8-s period waves. This supports the conclusion that comparable directional estimates can be obtained from sonar data in

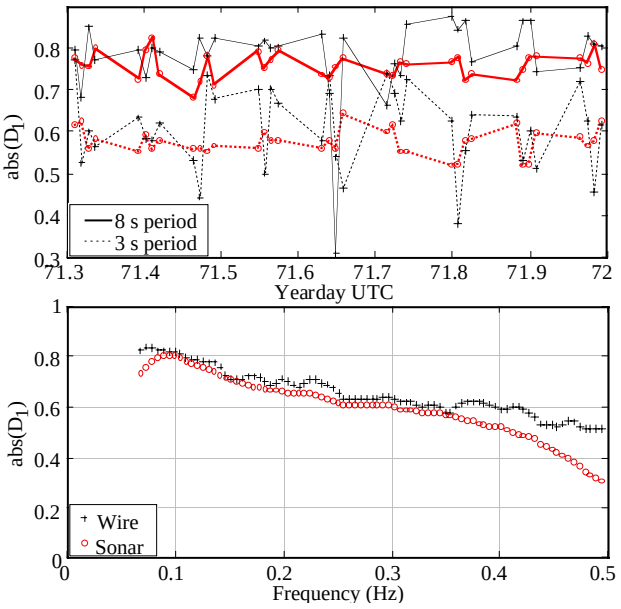

Fig. 17. Magnitudes of the first directional component from the wire data (crosses) and the four-beam sonar analysis (circles). This is a measure of the direcitonal spread. (top) Time-series of the magnitudes for 8 s (solid connecting lines) and 3 s waves. Note that the wire values scatter much more in time. (bottom) Time-averaged magnitudes versus frequency. The agreement is quite good between 0.08 and 0.35 Hz (for 3–12-s periods).

one quarter the time required from wires. While the correspondance between observed and estimated error levels is encouraging, there are some surprising yet consistent trends in the results, suggesting that there is more to be understood.

6. Summary

The quick directional analysis provides estimates of the first four circular Fourier components of the directional distribution of surface waves, from relatively short time segments. The RMS angular error of the first directional component, or momentum vector, ranges from 7° to 4° in each frequency bin (Δf = 1/64s) over 3 to 8 second period waves, using 12.8 minute data segments. To achieve a comparable error level with tilt and roll measurements requires about an hour of averaging time. This quick yet robust estimator for the wave directionality should prove useful for investigations of both the effects of wind variations on the evolution of the wavefield, and the effect of the wavefield on the wind stress.

Acknowledgments. This work was supported by the Physical Oceanography division of the Office of Naval Research, contracts N00014-90-J-1285 and N00014-93-1-0359. I would like to thank A. Plueddemann and R. Weller for the wind data; R. Pinkel for useful discussions; E. Slater, L. Green, M. Goldin, and C. Neely for making the instruments work, and the crew of *FLIP* for helping us deploy our instruments at sea.

REFERENCES

Abramowitz, M., and I. A. Stegun, *Handbook of Mathematical Functions*, pp. 1046, Dover, New York, 1965.

Crawford, C. B., and D. M. Farmer, On the spatial distribution of ocean bubbles, *J. of Geophys. Res.*, *92*, 8231-8243, 1987.

Goldstein, R. M., R. Li, J. A. Smith, R. Pinkel, and T. P. Barnett, Remote sensing of ocean waves: the surface wave process program experiment, *J. of Geophys. Res.*, *99*, 7945-7950, 1994.

Herbers, T. H. C., and R. T. Guza, Estimation Of Directional Wave Spectra From Multicomponent Observations, *Journal Of Physical Oceanography*, *20*, 1703-1724, 1990.

Krogstad, H. E., R. L. Gordon, and M. C. Miller, High-resolution directional wave spectra from horizontally mounted acoustic Doppler current meters, *Journal of Atmospheric and Oceanic Technology*, *5*, 340-352, 1988.

Longuet-Higgins, M. S., D. E. Cartwright, and N. D. Smith, Observations of the Directional Spectrum of Sea Waves Using the Motions of a Floating Buoy, in *Ocean Wave Spectra: Preceedings of a Conference*, Sciences, N. A. o. (Eds.), 111-132, Prentice-Hall International, Inc., London, 1963.

Pinkel, R., and J. A. Smith, Open Ocean Surface Wave Measurement Using Doppler Sonar, *Journal of Geophysical Research*, *92*, 12967-12973, 1987.

Pinkel, R., and J. A. Smith, Repeat-Sequence Coding For Improved Precision Of Doppler Sonar And Sodar, *Journal Of Atmospheric And Oceanic Technology*, *9*, 149-163, 1992.

Smith, J. A., Doppler Sonar and Surface Waves: Range and Resolution, *J. Atm. and Ocean. Tech.*, *6*, 680-696, 1989.

____, Observed Growth of Langmuir Circulation, *Journal of Geophysical Research*, *97*, 5651-5664, 1992.

____, Performance Of A Horizontally Scanning Doppler Sonar Near Shore, *J. Atmos. Oceanic Technol.*, *10*, 752-763, 1993.

Theriault, K. B., Incoherent Multibeam Doppler current profiler performance. Part I: estimate variance., *Journal of Ocean Engineering*, *OE-11*, 7-15, 1986.

Thorpe, S., Bubble clouds: a review of their detection by sonar, of related models, and of how K_V may be determined. *Oceanic Whitecaps and their role in air-sea exchange processes*, E. C. Monahan and G. M. Noicall, Eds., D. Reidel, 57-68, 1986.

Thorpe, S., and A. J. Hall, The characteristics of breaking waves bubble clouds, and near-surface currents observed using side-scan sonar., *Continental Shelf Research*, *1*, 353-384, 1983.

Trevorrow, M. V., and D. M. Farmer, The Use Of Barker Codes In Doppler Sonar Measurements, *Journal Of Atmospheric And Oceanic Technology*, *9*, 699-704, 1992.

Weller, R. A., M. A. Donelan, M. G. Briscoe, and N. E. Huang, Riding the Crest: A Tale of Two Wave Experiments, *Bull. Amer. Meteor. Soc.*, *72*, 163-183, 1991.